A mixture of hidden Markov models to predict the lymphatic spread in head and neck cancer depending on primary tumor location

Yoel Perez Haas[1,2], Roman Ludwig[1,2*], Julian Brönnimann[1,2], Esmée Lauren Looman[1,2], Panagiotis Balermpas[2], Sergi Benavente[11], Adrian Schubert[3,4,7], Dorothea Barbatei[8], Laurence Bauwens[8], Jean-Marc Hoffmann[2], Olgun Elicin[3], Matthias Dettmer[6,10], Bertrand Pouymayou[2], Roland Giger[4,5], Vincent Grégoire[8], Jan Unkelbach[1,2]

[1]Department of Physics, University of Zurich.

[2]Radiation Oncology, University Hospital Zurich.

[3]Department of Radiation Oncology, Bern University Hospital.

[4]Department of ENT, Head & Neck Surgery, Bern University Hospital.

[5]Head and Neck Anticancer Center, Bern University Hospital.

[6]Institute of Tissue Medicine and Pathology, Bern University Hospital.

[7]Department of ENT, Head & Neck Surgery, Réseau Hospitalier Neuchâtelois.

[8]Department of Radiation Oncology, Centre Léon Bérard.

[9]Department of Head and Neck Surgery, Centre Léon Bérard.

[10]Institute of Pathology, Klinikum Stuttgart.

[11]Departement of Radiation Oncology, Hospital Vall d'Hebron.

*Corresponding author(s). E-mail(s): roman.ludwig@usz.ch;

Contributing authors: yoel.perezhaas@usz.ch; jan.unkelbach@usz.ch;

Abstract

Purpose: to be done

Methods: to be done

Results: to be done

Conclusions: to be done

Introduction

Head and neck squamous cell carcinomas (HNSCCs) are known to spread through the lymphatic system often leading to metastases in the lymph nodes [1, 2]. To minimize nodal recurrences, lymph node levels (LNLs) at risk of harboring occult metastases are typically irradiated electively. Current guidelines for different tumor locations are based on the overall prevalence of nodal disease as reported in literature [1–3].

To personalize the prediction of the risk of occult metastases, given a patient's individual diagnosis, we previously published a large, multi-centric dataset where the lymphatic involvement per LNL is available for each patient[4, 5]. Building on this dataset, we introduced an interpretable hidden Markov model (HMM), trained to predict the risk for occult nodal disease, given an individual patient's diagnosis [6].

Personalized risk predictions could enable clinicians to safely reduce the elective clinical target volume (CTV-N), potentially decreasing treatment-related side effects that impair a patient's quality of life, without compromising the efficacy of the treatment [7].

Initially, separate models were trained for distinct tumor locations, such as the oropharynx and oral cavity. These tumor locations are also used in guidelines to define the elective target volumes [3]. However, this approach did not account for variations in lymphatic spread between subsites within these tumor regions. With data from more than 2700 patients available, we can now further analyze subsite specific spread patterns. Closer analysis showed that pooling subsites into a single model led to inaccurate predictions, as it failed to capture distinct lymphatic spread patterns. To resolve this, we propose using a mixture of HMMs, which allows us to model the lymphatic spread more accurately for tumors located near anatomical borders, such as those between the oropharynx and oral cavity (e.g., tumors in the palate).

Additionally, we extend the analysis to a broader mixture model that encompasses tumors of the oral cavity, oropharynx, hypopharynx, and larynx, resulting in further personalized predictions of lymphatic spread across these regions.

Data on Lymphatic Progression Patterns

For the analyses in this work, we used seven datasets from 5 institutions resulting in 2437 patients in total.

1. 287 oropharyngeal patients from the University of Zurich in Switzerland
2. 263 oropharyngeal patients from the Centre Léon Bérard in France
3. 327 oropharyngeal, larynx and oral cavity patients from the Inselspital Bern in Switzerland
4. 276 oropharyngeal, larynx and oral cavity patients from the Centre Léon Bérard in France
5. 273 oropharyngeal, larynx and oral cavity patients from the University of Zurich in Switzerland
6. 164 oropharyngeal patients from the Hospital Vall d'Hebron in Spain (not yet public)
7. 847 hypopharynx, larynx and oral cavity patients from University Medical Center Groningen (not yet public)

Patients with glottic laryngeal cancer (C32.0) at tumor stages T0 and T1 have been excluded from analysis because these stages, by definition, do not exhibit lymphatic involvement [need source from Panos]. The datasets 1-4 are publicly available as CSV tables [5, 8] and can be interactively explored on LyProX. For each patient the primary tumor subsite is reportd and each indicidual LNL is reported as either metastatic or healthy given the available diagnostic modalities, which include pathology after neck dissection in some patients. In this work we will stratify the tumor locations into different ICD codes which are depicted in figure 1.

The prevelance of involvement in LNLs I, II, III, IV and V is shown in figure 2. The involvement is stratified per tumor subsite and t-stage. The figure illustrates the variations in LNL involvement between subsites within oral cavity (blue), oropharynx (green), hypopharynx (red) and larynx (orange). The involvement pattern presents a continuous change over the tumor subsites. Where tumors in the oral cavity show the most prominent LNL I involvement. As the tumor location moves towards the oropharynx LNL II involvement increases. Moving the tumor location further in caudal direction towards the hypopharynx increases LNL III involvement while LNL I and II involvement decrease. Larnygeal tumors show the least LNL I involvement.

Unilateral Model for Lymphatic Progression

In this chapter we will briefly summarize unilateral model for ipsilateral lymph node involvement introduced in Ludwig et al. [6], presenting the notation which is then needed to extend the HMM to a mixture model encompassing multiple tumor subsites.

The HMM describes each LNL $v \in 1, 2, ..., V$ by a binary random variable corresponding to the status of the LNL; healthy (0) or involved (1). The entire state of a patient with V LNLs is defined by the V-dimensional vector $\mathbf{X} = [X_1, X_2, ..., X_V]$. In the HMM, a patient's involvement is modeled over time t. Thus, a patient's state of

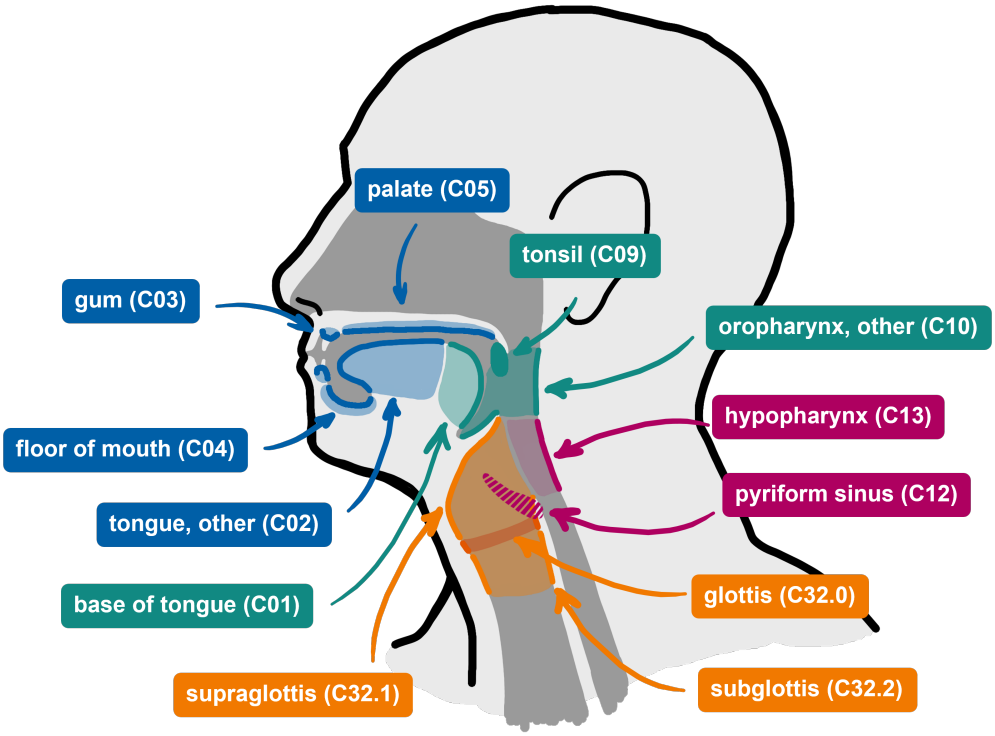

Figure 1: Anatomical sketch of the tumor subsites and their corresponding ICD-10 codes. Subsite C06 "other parts of mouth" has not been included. Further the The tumor locations are color coded in the following pattern: blue-oral cavity, green-oropharynx, red-hypopharynx, orange-larynx.

lymph node involvement $\mathbf{X}[t]$ evolves over discrete time steps t. Let us enumerate all 2^V possible states, representing all combinations of LNL involvement. In this paper, we consider ipsilateral LNLs I, II, III, IV and V, which amounts to 32 possible states. The HMM is then specified by a transition matrix $\mathbf{A}$:

$$\mathbf{A} = (A_{ij}) = P\left(\mathbf{X}[t+1] = \xi_j \mid \mathbf{X}[t] = \xi_i\right) \tag{1}$$

whose elements A_{ij} contain the conditional probabilities that a state $\mathbf{X}[t] = \xi_i$ transitions to $\mathbf{X}[t+1] = \xi_j$ over one time step. The transition matrix is specified and parameterised via the graphical model shown in figure 3. The red arcs in the graph of figure 3 are associated with the probability that the primary tumor spreads directly to a LNL (parameters b_v). The blue arcs describe the spread from an upstream LNL – given it is already metastatic – to a downstream level (parameters $t_{v \to v+1}$).

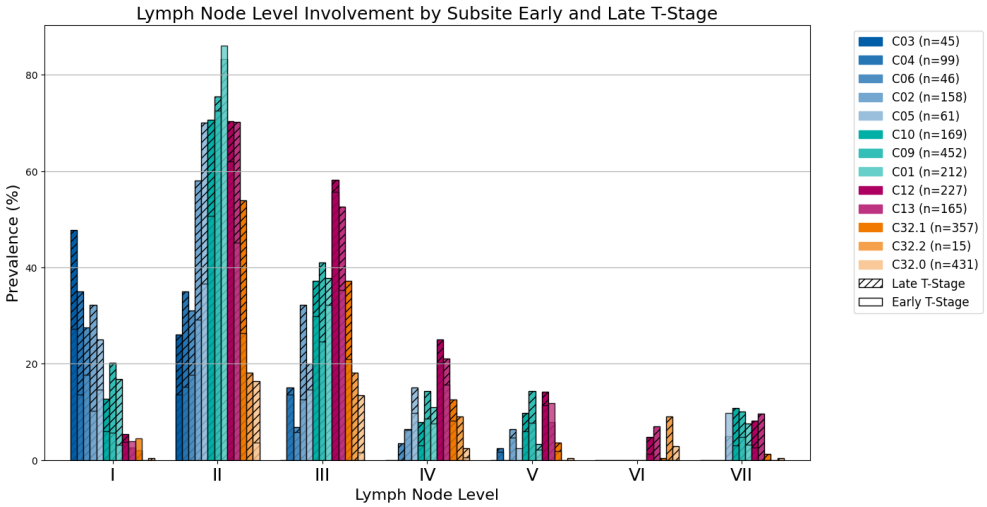

Figure 2: Prevalence of ipsilateral LNL involvement stratified by subsite. The subsites are sorted in natural order to represent the continuously changing LNL involvement. The different tumo locations are color coded, where oral cavity subsistes are depicted in blue, larynx in green, hypopharynx in red and larynx in orange. The patient data is further stratified in early t-stage (0-2) and late t-stage (3-4). The legend furter specifies the number of patients in each subsite. For glottis (C32.0) early t-stage only includes T2.

Now, let π be the *starting distribution*

$$\pi = (\pi_i) = P\left(\mathbf{X}[0] = \xi_i\right) \tag{2}$$

denoting the probability to start in state ξ_i at time step 0. Assuming that every patient started with all LNLs being healthy, we set π_i to zero for all states except the completly healthy state $\xi = (0, 0, 0, 0, 0)$, which has probability one.

Using the quantities introduced so far, the probability $P\left(\mathbf{X}[t] = \xi_i\right)$ to be in state ξ_i in time step t can now be conveniently expressed as a matrix product:

$$P\left(\mathbf{X}[t] = \xi_i\right) = \left(\pi \cdot \mathbf{A}^t\right)_i \tag{3}$$

This evolution implicitly marginalizes over all possible paths to arrive at state ξ_i after t time-steps. Additionally, we must marginalize over the unknown time of diagnosis using a time-prior $P_T(t)$ which is defined by a binomial distribution. The t-stage of the tumor can be included in the model by choosing different parameterizations of the binomial distribution, considering that a tumor in late t-stages was diagnosed later than a tumor in early t-stages, therefore shifting the probability of diagnosis to later time steps. This finally defines the probability distribution over all states of lymph node involvement.

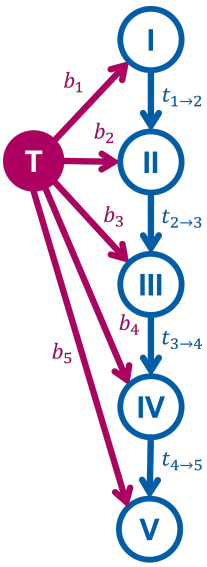

Figure 3: Parametrized graphical model of the lymphatic network considering four LNLs. Blue nodes represent the hidden states of LNLs X_v, while the red one is the tumor. Arcs represent possible routes of metastatic spread, associated with a probability.

$$P\left(\mathbf{X} = \xi_i \mid \theta, \mathbf{T}\right) = \sum_{t=0}^{t_{\max}} P_T(t) \left(\pi \cdot \mathbf{A}^t\right)_i \tag{4}$$

where $\theta = \{b_v, t_{v\to v+1}\}$ denotes the set of all model parameters (7 in our case). Fortunately, the exact length and shape of this distribution has little impact as previously shown [6]. We set $t_{\max} = 10$ and $P_{\text{early}}(t)$ to a binomial distribution with parameter 0.3. Further details on the HMM can be found in Ludwig et al. [6] and Ludwig [9].

With equation 4 we can compute the probability of a patient being in any state ξ_i. To train the model, we assume that the observed diagnoses in our dataset $\mathbf{D}$ directly reflect the underlying hidden states $\mathbf{X}$ of the patient. Thus, learning the model parameters corresponds to maximizing the probability of observing the dataset $\mathbf{D}$:

$$P\left(\mathbf{D} \mid \theta\right) = \prod_{k}^{K} P\left(\mathbf{X}_k = \xi_i \mid \theta, T_k\right) \tag{5}$$

In equation 5 we compute the likelihood of observing the diagnosis of each patient k, i.e. t-stage T_k and involvement $\mathbf{X}_k = \xi_i$.

Risk Estimation

The goal of the HMM is to predict the risk of occult metastases in LNLs, given a patient's diagnosis. In this framework this corresponds to computing the probability of a hidden state $\mathbf{X} = \xi_i$ given the observed diagnosis $\mathbf{Z}$ and the model parameters θ. With Baye's theorem we can compute this probability as follows:

$$P(\mathbf{X} = \xi_i \mid \mathbf{Z}, \theta) = \frac{P(\mathbf{Z} \mid \mathbf{X} = \xi_i, \theta) P(\mathbf{X}_k = \xi_i \mid \theta)}{P(\mathbf{Z} \mid \theta)} \tag{6}$$

where $P(\mathbf{Z} \mid \theta)$ is the marginal likelihood of the data, which can be computed by summing over all possible hidden states ξ_i:

$$P(\mathbf{Z} \mid \theta) = \sum_{\xi_i} P(\mathbf{Z} \mid \xi_i, \theta) P(\xi_i \mid \theta) \tag{7}$$

With this we can compute the probability for each hidden state and subsequently we can compute the probability for each LNL v to be involved given the diagnosis $\mathbf{Z}$ and the model parameters θ by summing over all possible hidden states $\xi_{i,v}$ where the LNL v is involved:

$$P(X_v = 1 \mid \mathbf{Z}, \theta) = \sum_{\xi_{i,v}} P(\mathbf{X} = \xi_i \mid \mathbf{Z}, \theta) \tag{8}$$

As opposed to the model training, we do not assume anymore that the diagnoses correspond to the hidden states. Instead, we consider the sensitivity and specificity of the diagnostic modalities used to determine the involvement of LNLs. Enabling the uncertainty originating from diagnostic modalities to be considered in the model. Here we chose the sensitivity of 0.81 for clinical modalities corresponding to the literature value for imaging modalities [10] and specificity of 1.0, indicating that all positively diagnosed LNLs are indeed involved.

Mixture Model for Lymphatic Spread

Primary tumors at different subsites exhibit distinct lymphatic spread patterns. This presents a challenge when attempting to generalize predictive models across subsites. One approach, as introduced in [11], uses a Hidden Markov Model (HMM) trained specifically for oropharyngeal cancer. However, extending this model to other subsites would either require generalizing over several subsites or training a separate model for each. The former approach sacrifices precision, particularly for subsites with fewer patients, while the latter approach becomes computationally intensive and introduces large uncertainties for subsites with limited patient data, such as C04 (Floor of mouth) or C05 (Palate).

To address these challenges and exploit the anatomical similarities between nearby subsites, we introduce a mixture model that combines data from all subsites into

a single model. This model accounts for anatomical proximities, thereby improving predictive power while maintaining computational efficiency.

Mixture Model Formulation

The mixture model assumes that the data is generated by a set of M different lymphatic spread models. Each patient k, with their primary tumor in subsite $s \in (1, 2, \dots, S)$, is assumed to be generated by one specific model $m \in (1, 2, \dots, M)$ from this set of M models with probability π_m^s. These so-called *mixing parameters* $\pi^s = \{\pi_1^s, \pi_2^s, \dots, \pi_M^s\}$ must satisfy the condition

$$\sum_m^M \pi_m^s = 1, \quad \forall s$$

If we could record the componet m from which a patient k was drawn from, we could store this information in a binary latent vector ϵ_k. The vector ϵ_k has length M, with exactly the m-th element set to 1, indicating which model generated the patient's data, and all other elements set to 0. Thus, for patient k, the latent variable ϵ_k can be interpreted as a categorical indicator variable that encodes the assignment to one of the M lymphatic spread models. Typically in mixture models, this so-called *latent variable* is unknown. However, it can be inferred and is useful for inferring the models' parameters.

The joint probability of the observed data $\mathbf{D}$ (i.e., patient data) and the latent variables ϵ - sometimes called the *complete data likelihood* - is given by:

$$P(\mathbf{D}, \epsilon \mid \theta, \pi) = \prod_k^K \prod_m^M \left[\pi_m^{s_k} P(\mathbf{D}_k \mid \theta_m)\right]^{\epsilon_k^m} \tag{9}$$

Here:

- $\pi_m^{s_k}$ is the mixing coefficient for subsite s_k (where patient k has their tumor) and model m,
- $P(\mathbf{D}_k \mid \theta_m)$ is the likelihood of patient k's diagnosis, i.e. The involvement state $\mathbf{X}_k = \xi_i$ and t-stage T_k, given that it was generated by model m,
- θ_m represents the parameters of model m,
- ϵ_k^m is the latent variable that indicates patient k was generated by model m.

In contrast, the *incomplete data likelihood* marginalizes over all possible latent assignments to reflect the uncertainty about which model generated each patient's data:

$$P(\mathbf{D}, \mid \theta, \pi) = \prod_k^K \sum_m^M \pi_m^{s_k} P(\mathbf{D}_k \mid \theta_m) \tag{10}$$

Ultimately, we want to find the parameters which maximize this likelihood function for the given data.

Note the summation inside the product. This structure of mixture models makes naive inference difficult, because the logarithm of this quantity is expensive to compute and not easy to differentiate. Thus, inferring the latent assignment is helpful, because the complete data (log-)likelihood (equation 9) does not suffer from this shortcoming.

To infer the latent assignment ϵ_k, we start with its distribution, given the observed data and model parameters:

$$\gamma(\epsilon_k^m) := \mathbb{E}[\epsilon_k^m] = \frac{\pi_m^{s_k} P\left(\mathbf{D}_k \mid \theta_m\right)}{\sum_{j \leq M} \pi_j^{s_k} P\left(\mathbf{D}_k \mid \theta_j\right)} \tag{11}$$

This expectation value - often called the *responsibility* - describes the probability that patient k was generated by model m. It can be used to compute the expected complete data likelihood:

$$\mathbb{E}_\epsilon \left[P\left(\mathbf{D}, \epsilon \mid \theta, \pi\right)\right] = \prod_{k=1}^{K} \prod_{m=1}^{M} \left[\pi_m^{s_k} P\left(\mathbf{D}_k \mid \theta_m\right)\right]^{\gamma(\epsilon_k^m)} \tag{12}$$

This expected complete data likelihood has the same tractable form as equation 9 and thus allows us to infer both the mixing coefficients π as well as each component model's parameters θ_m using straightformward inference. Also, these two sets of parameters are the only ones used for the later risk prediction. The responsiblities $\gamma(\epsilon_k^m)$ are only used during inference.

In figure 4 the mixture coefficients are illustrated. Subsites with different spread patterns, such as Gum (C03) and Base of tongue (C01), are expected to get different model assignments. Nonetheless, the latent variables for two patients with the same diagnosis, i.e. same involvement ξ and and t-stage T, but different subsites are the same.

It is important to note that this mixture model algorithm diverges from the conventional formulation of mixture models as introduced in Bishop [12]. In Bishop's work, the mixture model is defined with a single set of mixture parameters π, implying that all data points are generated from the same mixture of models. In our approach, however, we categorize the data points (patients) into distinct cohorts (subsites), with each subsite characterized by its own set of mixture parameters. Consequently, we construct S separate mixture models, each possessing different mixture parameters while all models share the same underlying probability distributions, specifically the varying lymphatic spread models.

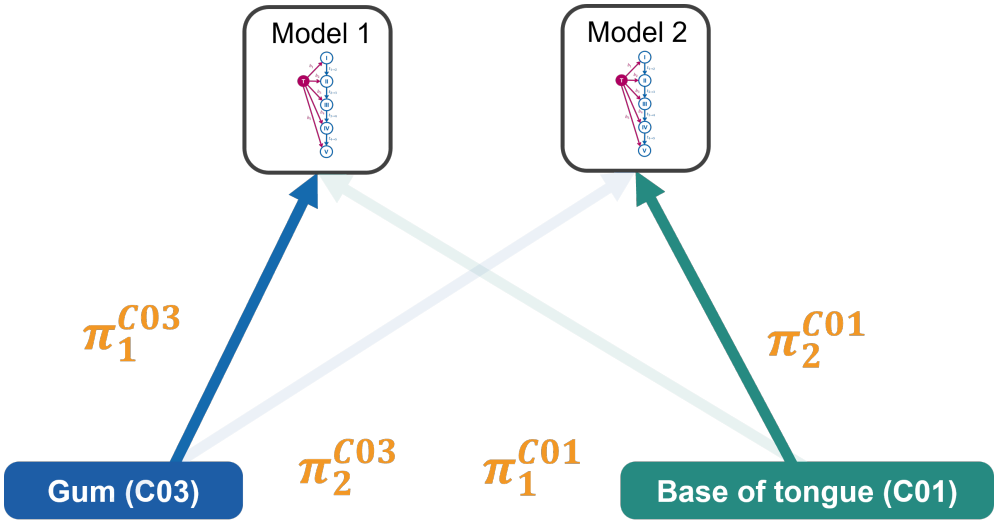

Figure 4: Illustration of mixture parameter assignment. Since Gum and Base of tongue express different spread patterns, the two models are expected to have different model assignments. The arrow visibility represents the value of the mixture parameter π, where the more visible the arrow, the larger the value for π

Expectation-Maximization (EM) Algorithm

To find the mixing coefficients π and all models' parameters θ_m that maximize equation 10, we follow an iterative approach called *expectation-maximization* or *EM-algorithm*. With arbitrarily initialized starting parameters, we alternate between the following two steps:

1. In the **E**xpectation step, we compute the responsibilities $\gamma(\epsilon_k^m)$, which represent the probabilities of a patient k originating from one of the models m, given the current estimates of θ and π, as given in equation 11.
2. During the **M**aximization step, we find a new set of parameters that maximize the new expected complete data likelihood (equation 12). For the mixture coefficients, we can even find an analytic solution to the new maximum:

$$\pi_m^s = \frac{1}{|K_s|} \sum_{k \in K_s} \gamma(\epsilon_k^m)$$

where we sum over the set of all patients K_s with their tumor in subsite s.
The models' new parameters are found by numerically maximizing the respective likelihood, weighted by the responsibilities:

$$\ln P(\mathbf{D}, \epsilon \mid \theta_m) = \sum_k^K \gamma(\epsilon_k^m) [\ln \pi_m^{s_k} + \ln P(\mathbf{D}_k \mid \theta_m)] \tag{13}$$

By iterating these steps, the EM algorithm is guaranteed to converge to a (local) maximum of the incomplete data likelihood (equation 10).

Uncertainty estimation

To estimate the uncertainty associated with both the model parameters and the resulting risk estimates, we employ a bootstrapping approach. Although more comprehensive sampling methods exist for the EM algorithm—such as the imputation-posterior (IP) algorithm, which samples from both model parameters and latent variables—we opt for a computationally more efficient alternative that still yields multiple estimates of all parameters.

Our resampling procedure involves the following steps:

1. Resample the observed data with replacement, maintaining the original number of samples per ICD code.
2. Fit the model to each resampled dataset.
3. Extract the model parameters and risk estimates from each fitted model.

This method enables a straightforward uncertainty analysis while avoiding the computational cost of more intensive sampling techniques.

Model Training Evaluation

In the following sections we will analyze the model training for three components first, considering Oral Cavity, Oropharynx and Hypopharynx data. Then we extend the model to four components, additionally including Larynx data. Both models will include LNLs I, II, III, IV and V. LNLs VI and VII are omitted for simplicity and since the prevalence for these LNLs never exceeds 11% (figure 2), meaning that the risk of involvement is low in most cases.

Three Component Mixture Model

We first evualuate the methodology for a mixture model with $M = 3$ components. We include the ICD codes as subsites for oral cavity, hypopharynx and oropharynx. In figure 5 the convergence of the negative log-likelihood and change in model parameters is depicted. After a random inizialization, the algorithm rapidly converges. The algorithm was stopped when the difference of log-likelihood between two iterations was below 0.01.

In figure 6, we visualize the resulting mixture coefficients π using a spatial representation, where the vertices of the triangle correspond to the three components. In figure 7, these mixture coefficients are presented in matrix form, with the y-axis representing the ICD codes, showing how the mixture components in each row add up to 1.

The spatial plot in figure 6 illustrates how the model assigns the three components to different tumor subsites. Component 0, located at the bottom right of the triangle,

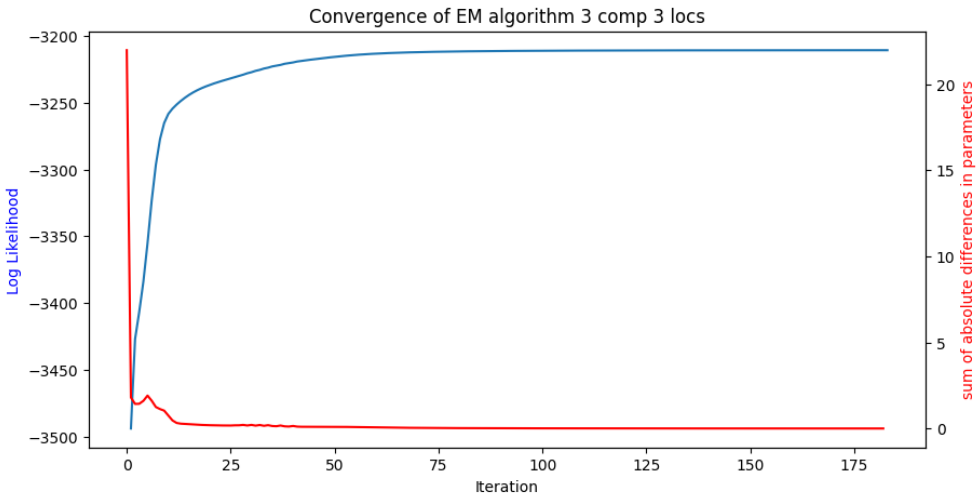

Figure 5: The y-axis on the left shows the negative likelihood convergence depicted in the blue line. The y-axis on the right shows the sum of absulte difference between all model parameters showing that the parameter values stabilize rapidly as well.

primarily characterizes hypopharyngeal subsites. Both hypopharyngeal subsites, piriform sinus (C12) and hypopharynx (C13), are strongly assigned to this component. Similarly, component 1, located at the bottom left, characterizes oral cavity subsites. For instance, the gum (C03), which has the highest LNL I involvement is fully assigned to this subsite. As subsites anatomically approach the oropharynx, their mixture coefficients for the oropharynx-like component, at the top of the triangle, increase. This is evident in the subsites C02 (tongue) and C05 (palate), which display a higher proportion of oropharyngeal influence in their mixture. These results conform well with the involvement patterns observed in the data in figure figure 2. The base of tongue subsite (C01), which exhibits the highest involvement of LNL II, is fully assigned to oropharynx-like component. Similarly, subsite C10, which includes several oropharyngeal regions, is assigned roughly 50% to the oropharynx-like component, with the remaining mixture distributed across the other two components, representing its large variation in spread patterns.

To evaluate the uncertainty in the model parameters, the bootstrapping approach introduced in section 11 has been applied. Specifically, we generated 200 bootstrap samples by resampling the observed data with replacement, maintaining the original number of samples per ICD code. For each bootstrap sample, the mixture model was re-fitted, and the resulting parameters were recorded. This process yielded a distribution of parameter estimates, allowing us to compute confidence intervals and assess the variability in the model's predictions.

The results of the bootstrapping analysis are shown in figure 8 and figure 9. The figure illustrates the variability in the mixture coefficients π for each subsite in the same representation as figure 6. The figure shows that the uncertainties match the

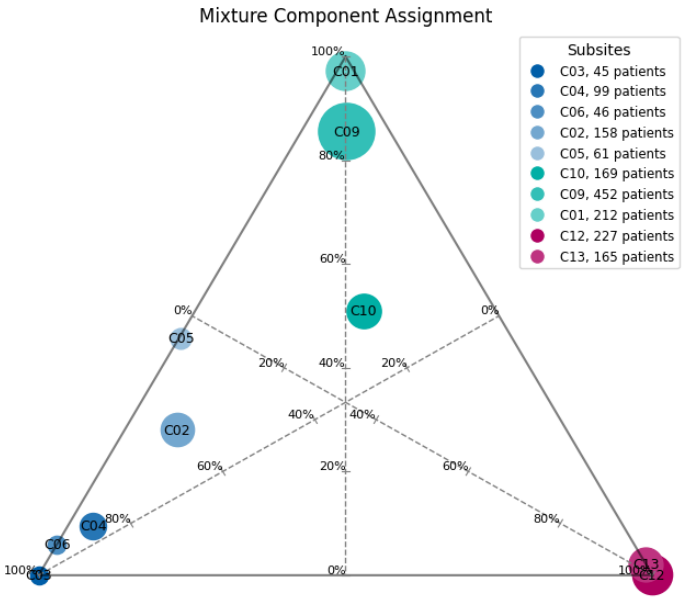

Figure 6: Assignment of each subsite to each of the three components. The closer a subsite is to a vertex, the more it is assigned to the corresponding component, with component 0 on the bottom right, 1 on the bottom left and 2 on the top. The size of the marker (area) corresponds to the number of patients in each subsite.

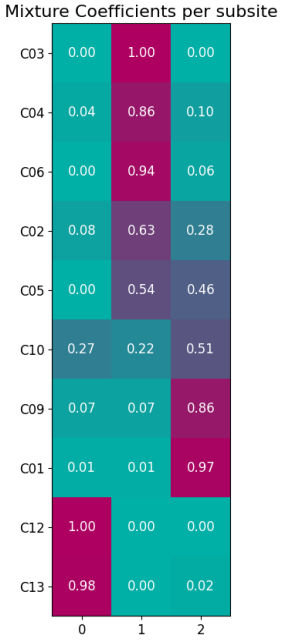

Figure 7: Matrix representation of component assignment. Each row of the matrix corresponds to each ICD code. The collums represent the three different components

continuity of the spread patterns. The base of tongue (C01) has most of its uncertainty along in between the oropharynx component and the hypopharynx component. Similarly, the hypopharynx subsite (C13) mostly presents uncertainty between these two components. The more general oropharnyx subsite (C10) shows more uncertainty in each components direction, due to its mixed spread pattern. The subsite for other pars of mouth (C03) however, only has uncertainty along the axis connecting the oropharyngeal component and the oral cavity componen, therefore never mixing with the hypopharynx-like component on the right. In figure figure 9 the asymmetry of the uncertainty is better depicted. E.g. the base of tongue (C01) subsite and the hypopharynx (C13) subsite have strongly asymmetric uncertainties. Further, the plot better characterizes the uncertainty in the palate subsite (C05), where the mixture and uncertainty is mainly in the oropharynx-like and the oral cavity-like components if we center the uncertainty around the optimal values instead of the mean values as it is depicted in figure 8.

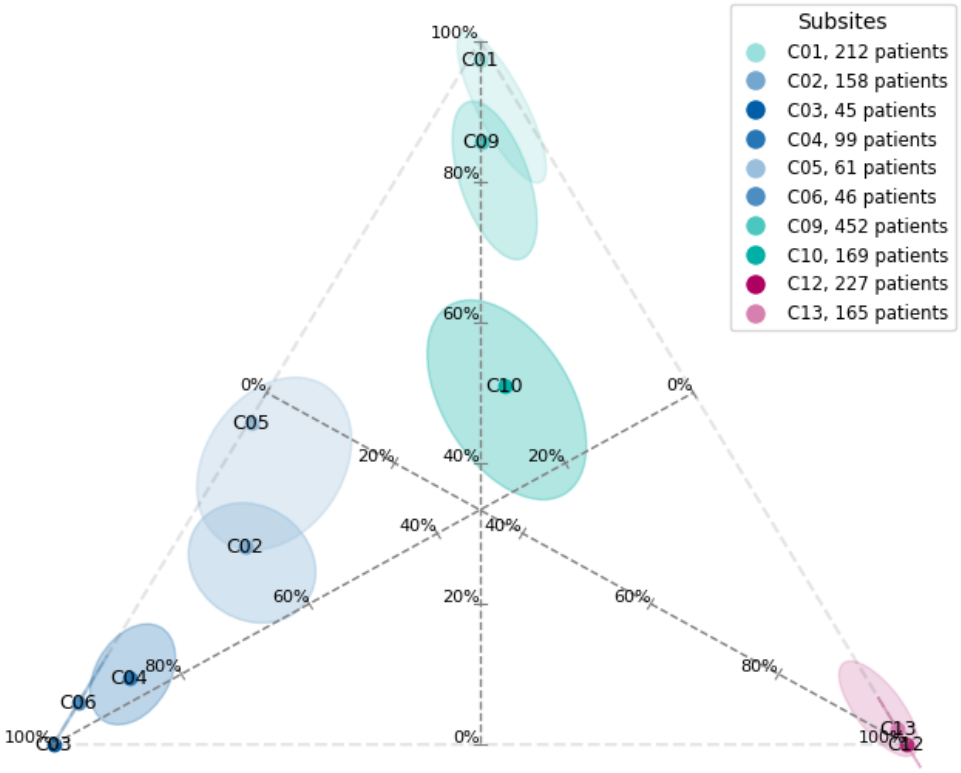

Figure 8: Variability in mixture coefficients π across bootstrap samples for each subsite. Where the dots represent the optimal values and the ellipses represent the 68% percentile centered around the mean value. The 68% percentile are computed assuming a 2D-gaussian distribution. However, with the bounds of 0 and 1 the sampled mixture coefficients do not exactly follow a gaussian distribution.

Additionally, the bootstrapping approach enables us to quantify the uncertainty in the model predictions for each subsite and LNL. To benchmark the model we analyze the predicted and observed prevalences for LNLs I, II, III, IV, and V. These predictions are stratified by tumor subsite and t-stage, providing a comprehensive view of the model's performance and its associated uncertainty.

In figure 10 we present the predictions for the oral cavity subsites C03 and C05. Here we can clearly see in figure figure 15a and figure 16c that the difference in prevalence is substantial, even though both subsites are grouped in the same tumor location. The model predicts a higher prevalence for LNL II in subsite C05 (palate) compared to subsite C03 (gum). This is consistent with the observed data, where the prevalence of LNL II involvement is higher for the palate than for the gum. However, the model only predicts a slightly higher prevalence for LNL I in subsite C03 compared to subsite

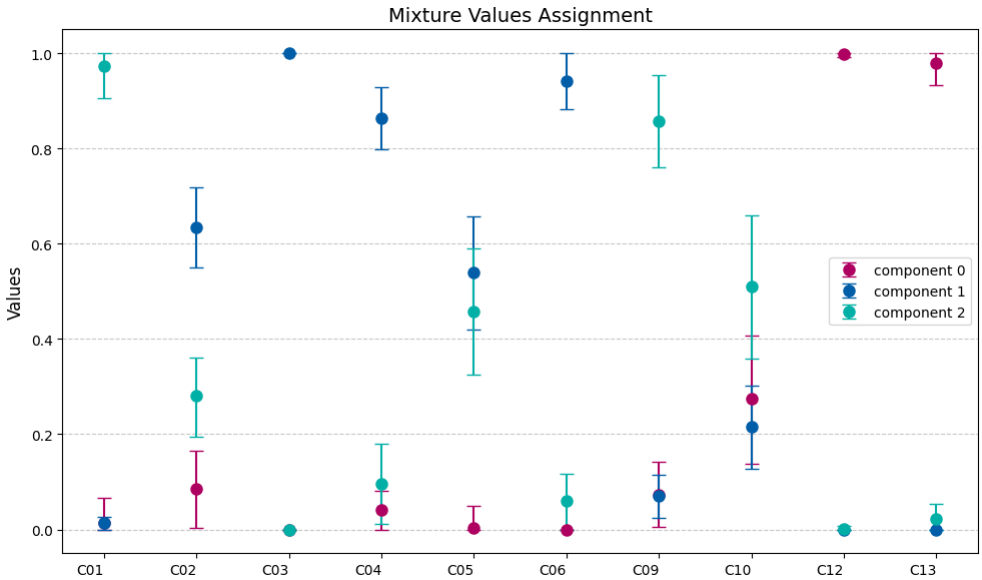

Figure 9: Variability in mixture coefficients π across bootstrap samples for each subsite. The dots represent the optimal values. The bars include 68% of all sample values centered around the optimal values.

C05. This is not consistent with the observed data, where the prevalence of LNL I involvement is significantly higher for the gum than for the palate. Thus, showing a limitation in the model to properly split these different involvements. In late t-stages, depicted in figure figure 16c and figure 16d, the model predicts a higher prevalence for LNL II in subsite C05 compared to the early t-stage, but not fully capturing the increase in prevalence. For subsite C03 the LNL II involvement is predicted to increase as well, capturing the increase in prevalence. However, for LNL I, while capturing the increase in prevalence, it does not optimally predict the prevalence, similarly to the early t-stage. For LNLs III, IV and V, the model consistently predicts the low prevalences observed in the data for both subsites.

In figure 11 we present the predictions for the oropharynx subsites C01 and C10. In figures figure 11a and figure 11b we can see that the model predicts a higher prevalence for LNL II in subsite C01 (base of tongue) compared to subsite C10 (oropharynx). This is consistent with the observed data. In figures figure 11c and figure 11d we can see that the model precisely captures the increased prevalence in late t-stage for both subsites. LNLs I, IV and V are predicted to have low prevalences for both subsites, but the model does not perfectly fit the predicted prevalences to the observed prevalences.

In summary, the mixture model successfully distinguishes between subsites, capturing the continuous variation in lymphatic spread patterns across tumor locations. However, the model's predictions are not always perfect. While it generally aligns with

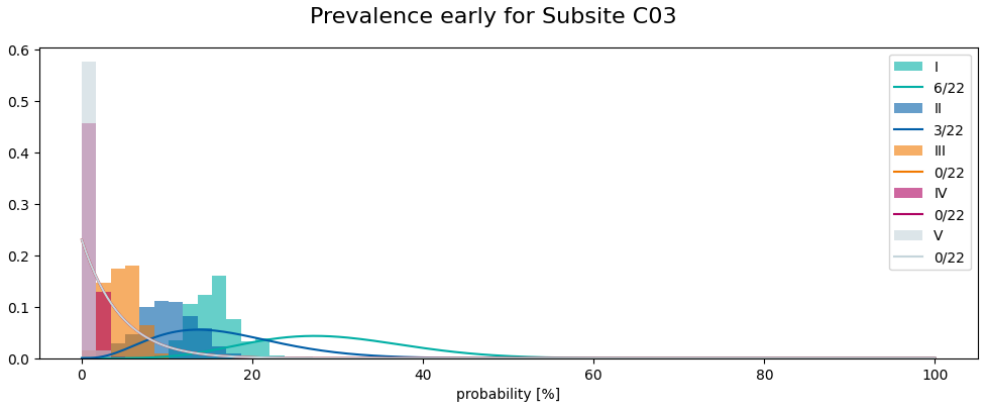

(a)

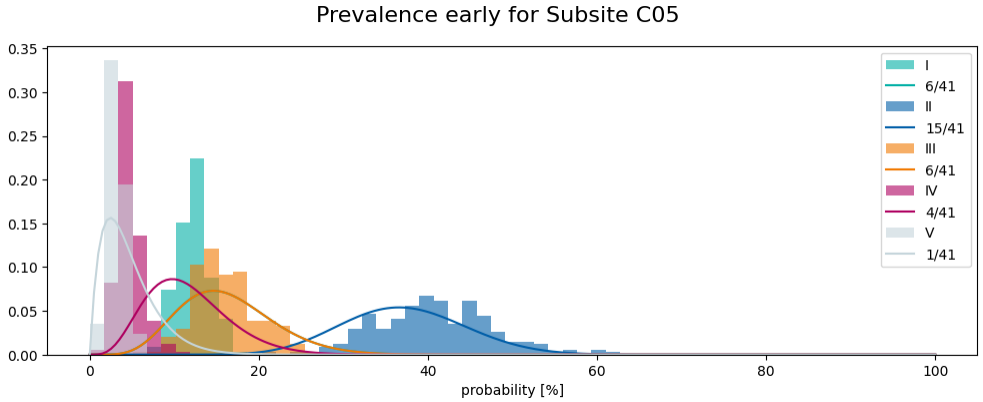

(b)

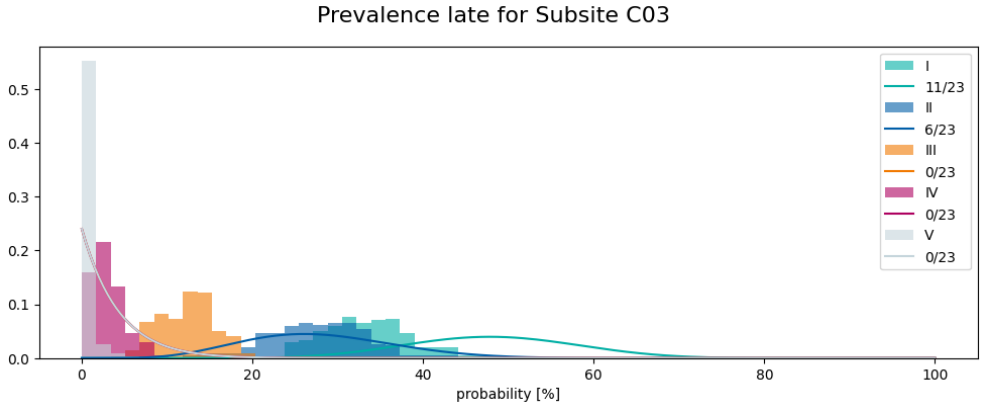

(c)

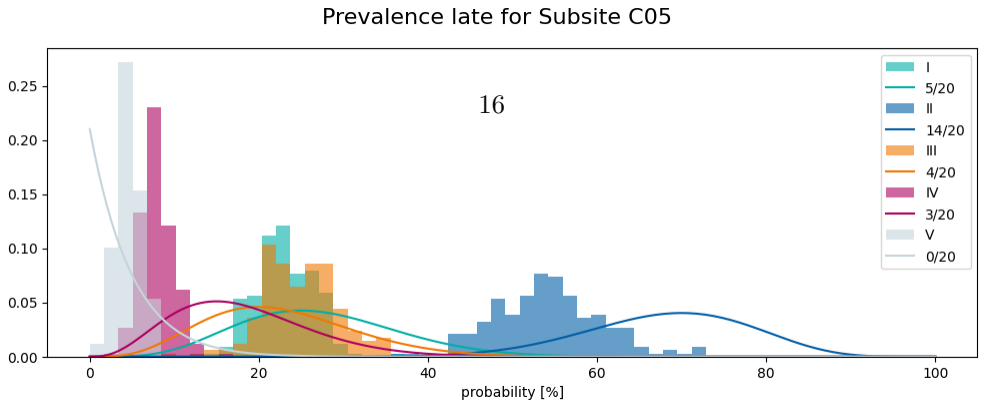

(d)

Figure 10: Observed prevalence (solid lines) and predicted prevalence (histograms) for subsites C03 and C05. Figures a and b show the prevalences for early t-stages. Figures c and d show the prevalences for late t-stages.

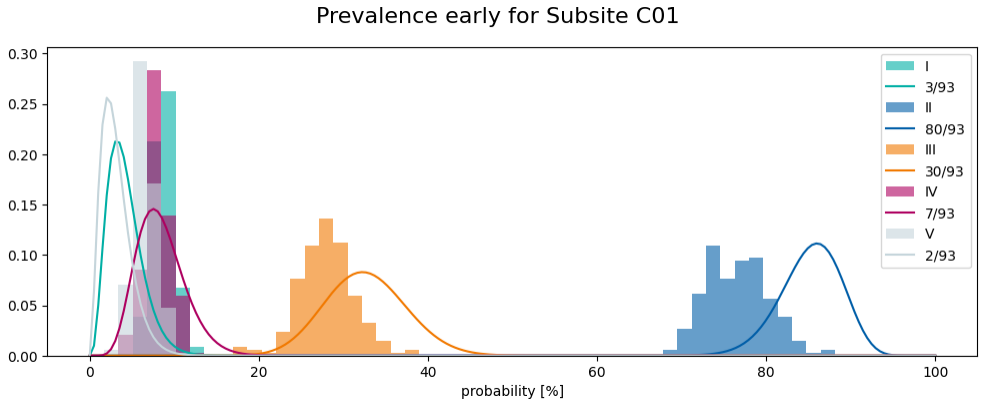

(a)

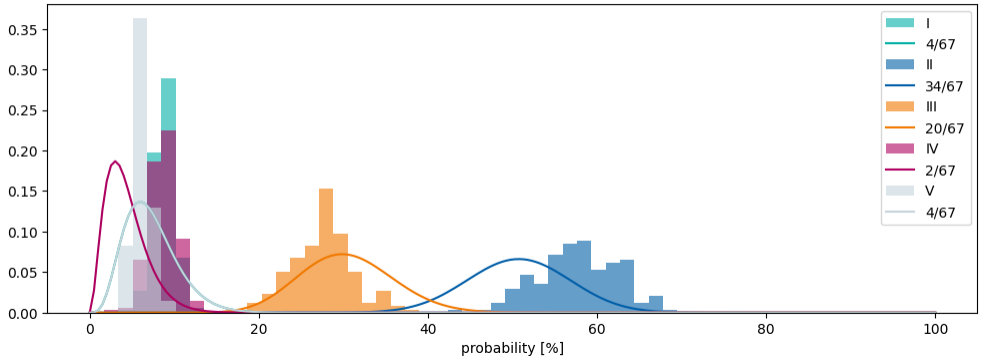

(b)

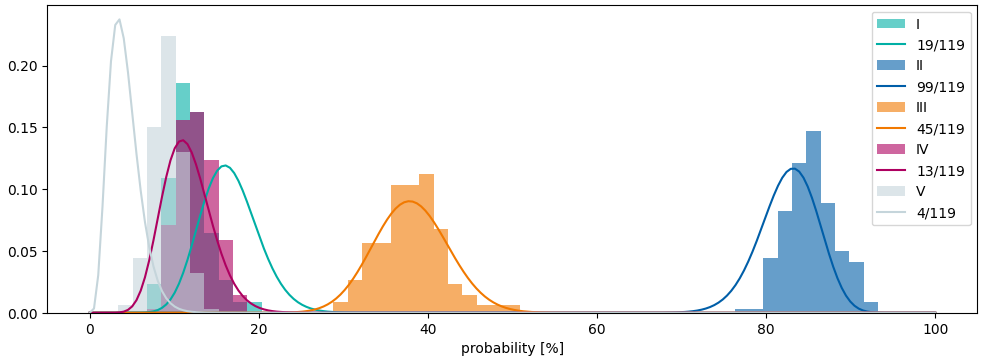

(c)

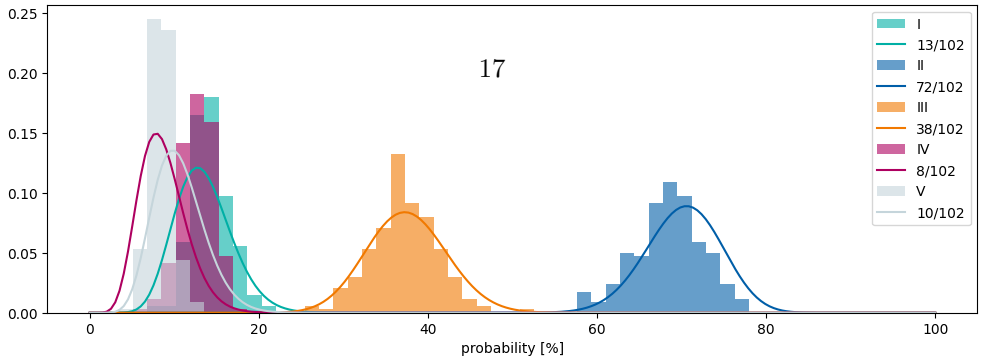

(d)

Figure 11: Observed prevalence (solid lines) and predicted prevalence (histograms) for subsites C01 and C10. Figures a and b show the prevalences for early t-stages. Figures c and d show the prevalences for late t-stages.

observed data, certain nuances, such as the higher prevalence of LNL I involvement in subsite C03 compared to C05, are not fully captured.

Four Component Mixture Model

We can extend the mixture model to include the larynx. The larynx patients are more finely divided into ICD codes C32.0, C32.1 and C32.2 as there is a notable difference between these ICD codes in figure 2.

Simlarly to the three component model, we can analyze the convergence over the iterations of the EM-algorithm. In figure 12 we can see that in this more complex model, the likelihood space becomes more complex as at around 200 iterations, the negative log-likelihood starts to increase faster again.

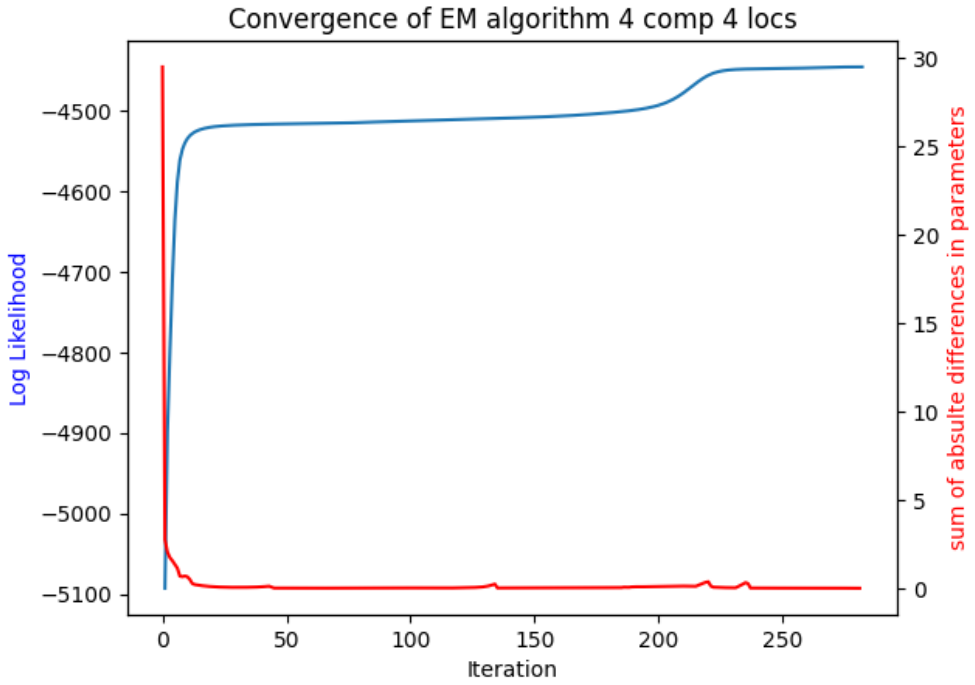

Figure 12: The y-axis on the left shows the negative likelihood convergence depicted in the blue line. The y-axis on the right shows the sum of absulte difference between all model parameters.

The component assignment is shown in figure 13. Similarly to the 3-component model the different tumor locations are assigned to a one of the components. In this case, the new component is used to model laryngeal subsites. The uncertainty of the assignments is shown in figure 14. The most striking differences are in subsites C03 and C12, which were formerly assigned to a single component. Now, C03 mixes with the

laryngeal component, while C12 is mixed with the laryngeal and the hypopharyngeal component. Another interesting observation is the mixture of the supraglottis subsite (C32.1) which is anatomically close to the hypopharynx. The model assigns a strong mixture of the larynx-like component and the hypopharynx-like component to this subsite. This is consistent with the observed data, where the supraglottis subsite has a high prevalence of LNL II and III involvement, which is also observed in the hypopharynx subsites. In contrast, the glottis subsite (C32.0) is strongly assigned to the laryngeal component, while the subsite C32.2 (subglottis) is assigned to the laryngeal component with little uncertainty. This is consistent with the observed data, where the glottis subsite has a much lower prevalence of involvement in any LNL. However, there is a strong t-stage dependency for this subsite.

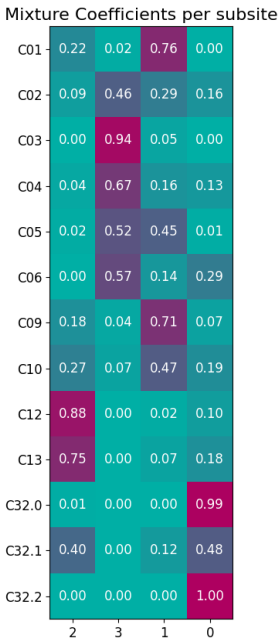

Figure 13: Matrix representation of component assignment. Each row of the matrix corresponds to each ICD code. The columns represent the four different components

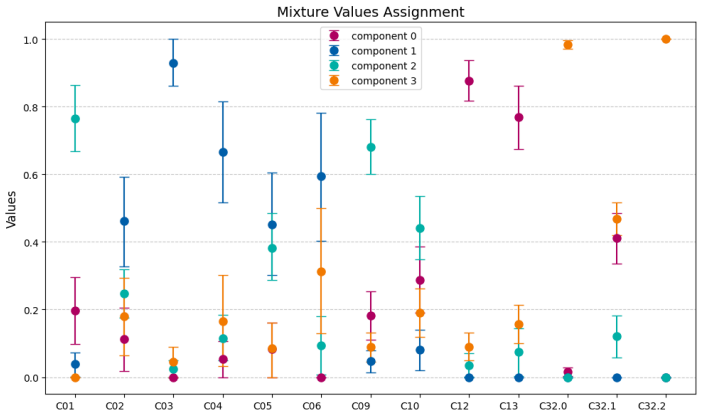

Figure 14: Assignment of each subsite to each of the four components. The closer a subsite is to a vertex, the more it is assigned to the corresponding component, with component 0 on the bottom right, 1 on the bottom left, 2 on the top left and 3 on the top right. The size of the marker (area) corresponds to the number of patients in each subsite.

Similarly to the three component model, we can analyze the predicted and observed prevalences for LNLs I, II, III, IV and V. We will first revisit the oral cavity subsites C03 and C05. to check, whether the additional component improves the model predictions. In figure 15 the predictions for the oral cavity subsites C03 and C05 are shown. The model now predicts a higher prevalence for LNL I in subsite C03 (gum) compared to subsite C05 (palate) for both early and

The predicted prevalences for for the laryngeal subsites C32.0 and C32.1 are shown in figure 16. Here, the large difference between early and late t-stages is clearly visible. For subsite C32.0 (glottis) the model predicts a very low prevalence for LNL I, II and III in early t-stages, which is consistent with the observed data. For late t-stages, the model captures the increased involvement probabilities for LNLs II and III. For subsite C32.1 (supraglottis) the model overestimates the prevalence for LNLs II and III in early t-stages and slightly underestimates their prevalence in late t-stages.

The model parameters for the larynx-like component are shown in figure 17. The parameter that governs the impact of t-stage p_late is estimated around 1. Therefore, the model maximizes the increase of risk of involvement for late t-stages to capture the large difference in prevalence between early and late t-stages.

Model Predictions

Given the model parameters, we can compute the risk of occult metastases given a patient's diagnosis. The model can be applied to predict the risk of involvement for each LNL, given the patient's t-stage and primary tumor subsite.

The risk predictions are computed by applying the equation 8 to each component and subsequently mixing the results using the mixture coefficients π. The risk of involvement for each LNL v in subsite s is given by:

$$P(X_v^s = 1 \mid \mathbf{D}, \theta) = \sum_{m=1}^{M} \pi_m^s P(X_v = 1 \mid \mathbf{D}, \theta_m) \tag{14}$$

where s is the subsite and θ_m are the parameters of model component m.

For all estimates we will set a 5% threshold for the risk of involvement. This means that if the model predicts a risk of involvement of 5% or higher, we will consider the LNL to be at a "high" risk of involvement and should be irradiated. Consequently all LNLs with a risk of involvement below 5% will be considered to be at a "low" risk of involvement and should not be irradiated. This allows us to compare the model predictions with the current clinical guidelines for elective irradiation of LNLs.

In the following sections we will analyze the model predictions for the four component model only and for selected clinical diagnoses.

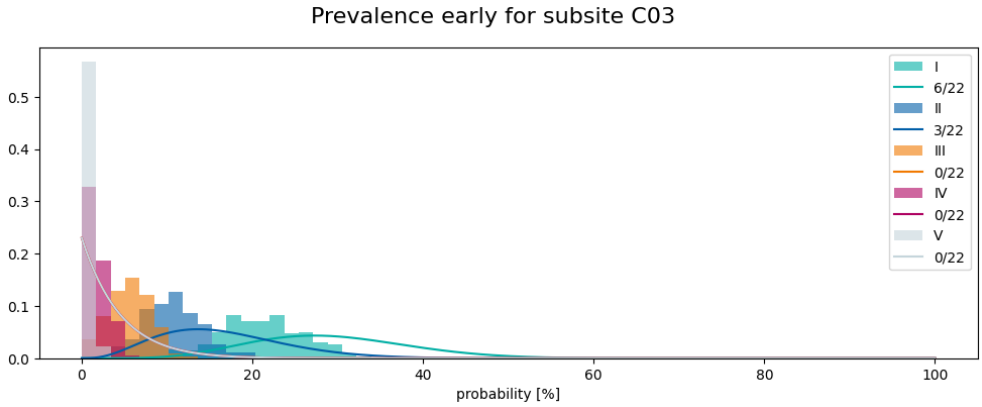

(a)

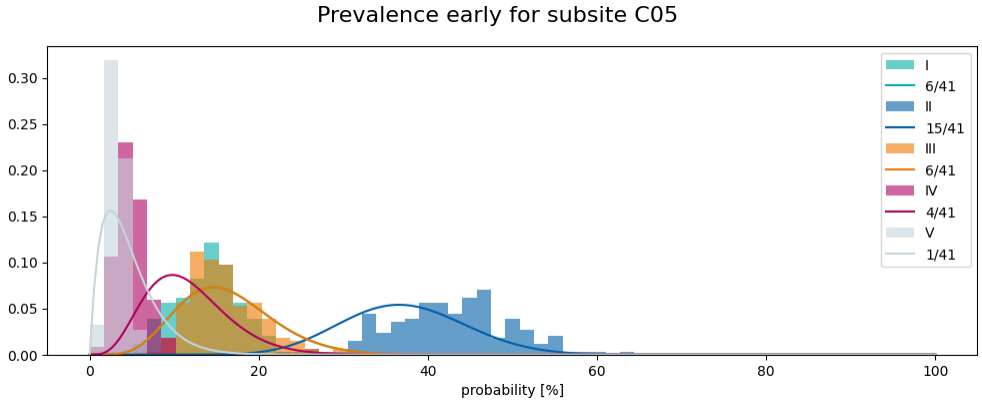

(b)

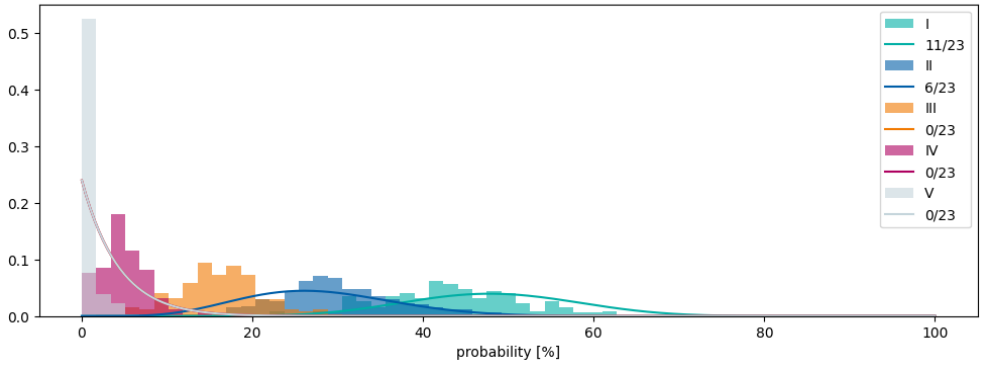

(c)

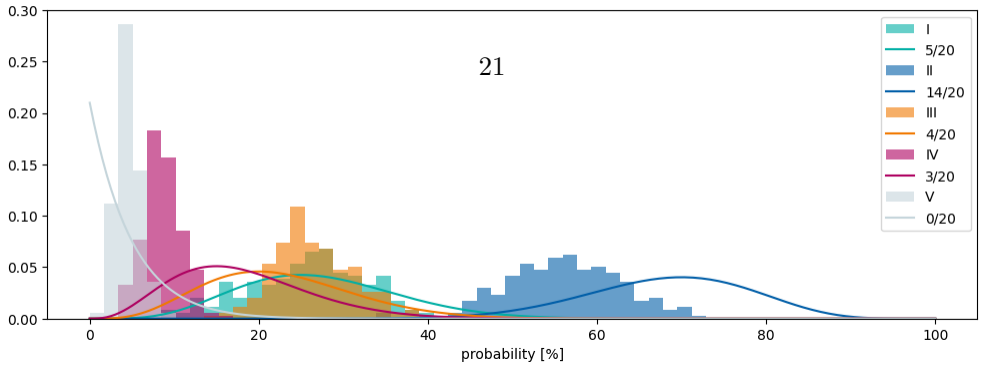

(d)

Figure 15: Observed prevalence (solid lines) and predicted prevalence (histograms) for subsites C03 and C05. Figures a and b show the prevalences for early t-stages. Figures c and d show the prevalences for late t-stages.

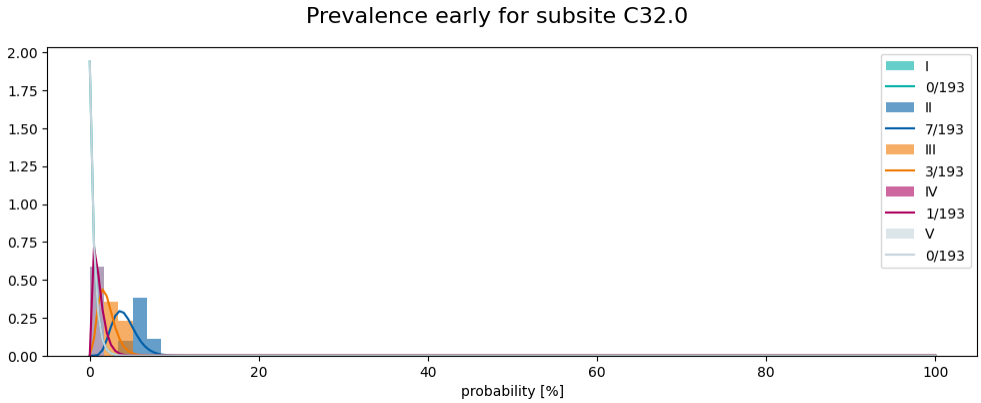

(a)

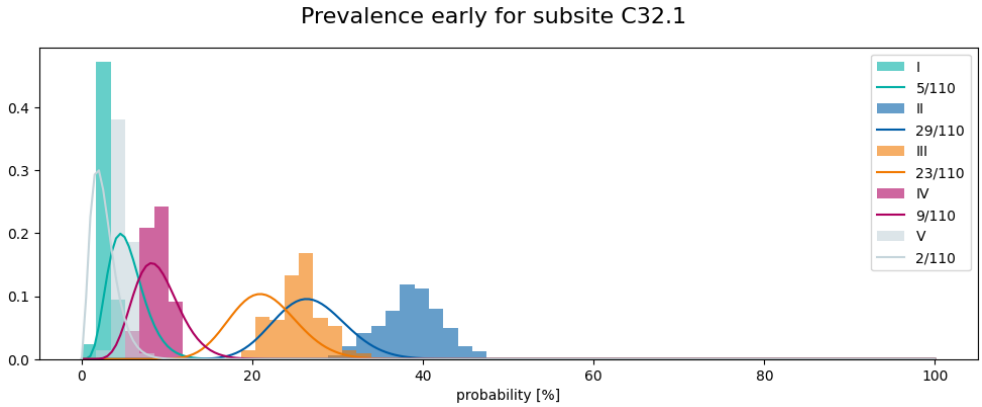

(b)

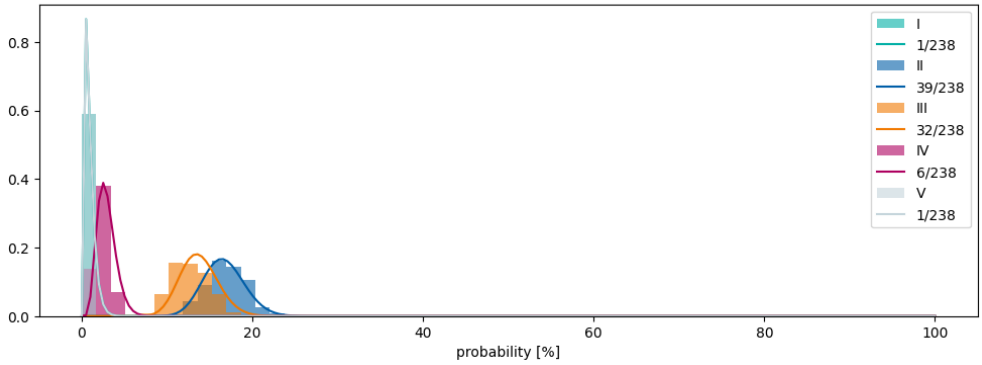

(c)

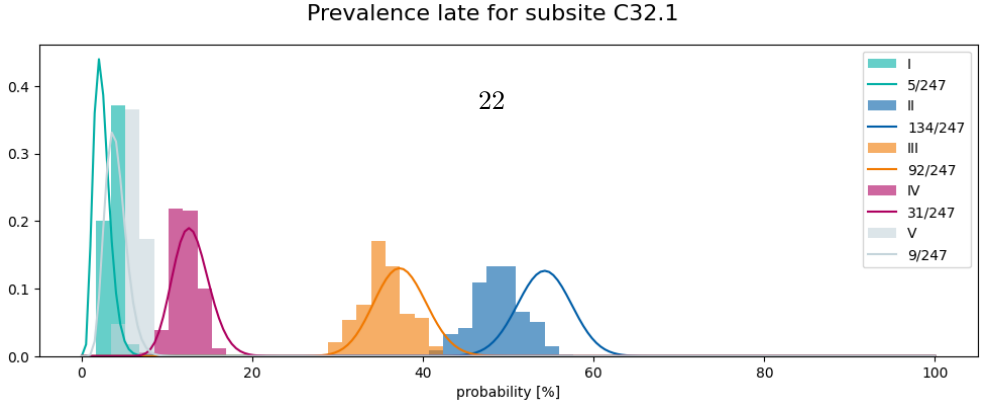

(d)

Figure 16: Observed prevalence (solid lines) and predicted prevalence (histograms) for subsites C32.0 and C32.1. Figures a and b show the prevalences for early t-stages. Figures c and d show the prevalences for late t-stages.

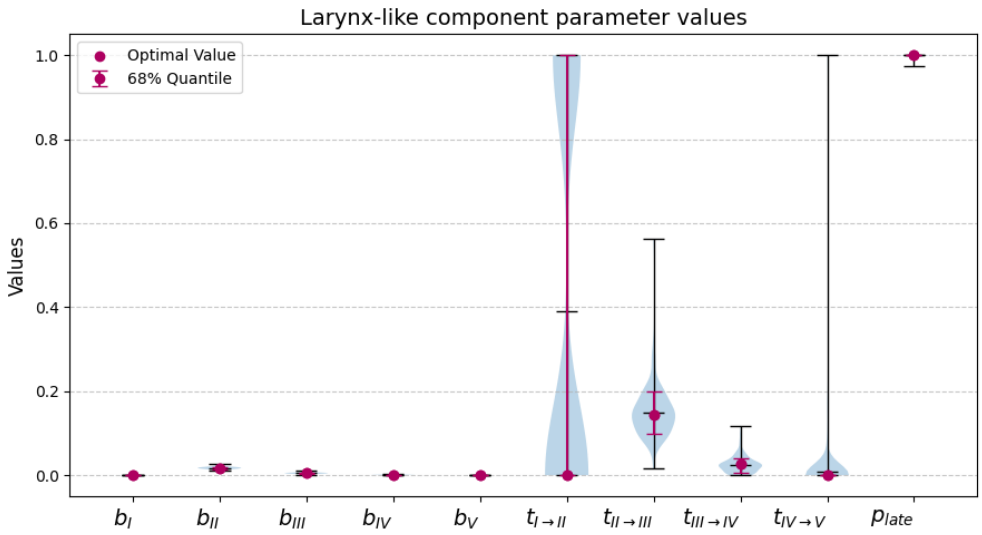

Figure 17: Model parameters for the larynx-like component. The optimal value and the 68% percentile around the optimal value are marked in red. The mean values and extreme values are indicated by the black bars.

Oral cavity

Oral cavity tumors typically spread to LNLs I, II and III as shown in figure 2. Consequently, the clinical guidelines recommend irradiating LNLs I, II, III for all tumors, irrespective of t-stage and even if there is no LNL involvement [3].

We first analyze the risk predictions for the case where we clinically diagnose no positive LNLs

In figure 18 we can see that the model predicts different risks of involvement for each subsite. For subsite C03 (gum), predicts a higher risk of involvement for LNL I. In subsites C02 (tongue) and C05 (palate), the model predicts an above threshold risk of involvement for LNL II. While for subsites C02 (tongue) and C06 (other parts of mouth) all LNLs stay below the 5% threshold. Thus, the model would propose three different treatment plans for these subsites, with C03 (gum) LNL I, C02 (tongue) LNL II and C05 (palate) LNL II being irradiated, while C04 (floor of mouth) and C06 (other parts of mouth) would not need elective irradiation at all, which is a major deviation from the clinical guidelines which irradiate LNLs I, II and III for all oral cavity subsites.

Appendix

Here I will probably add more figures such as all component parameter estimates and their uncertainties.

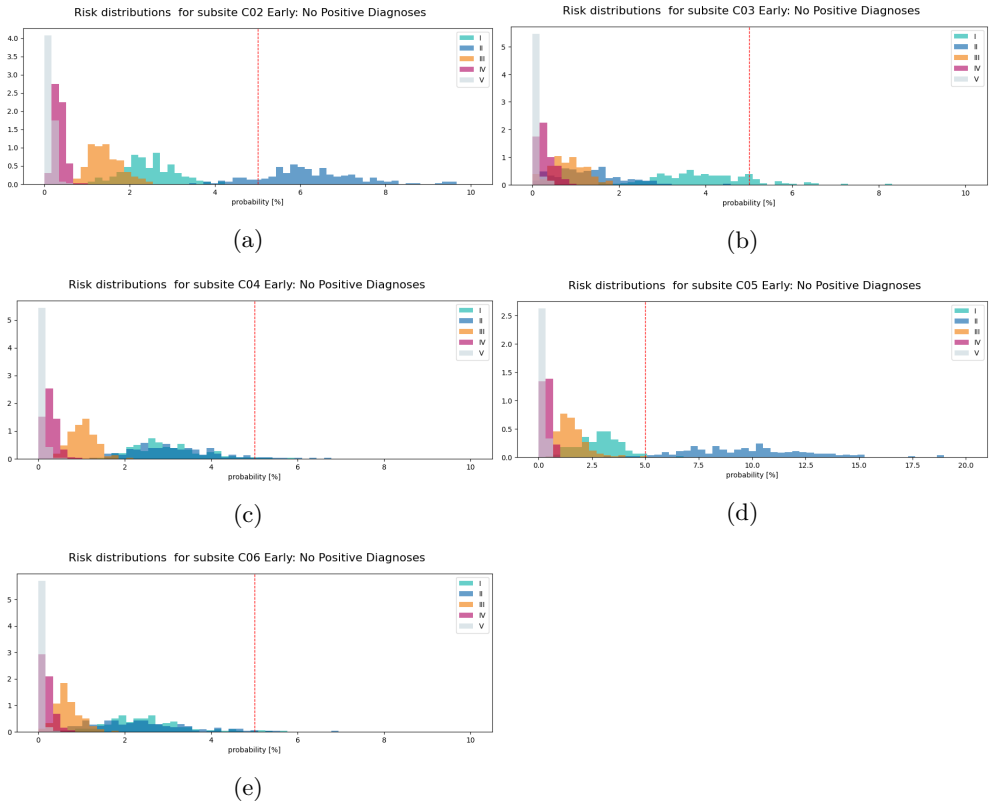

Figure 18: Probability of occult metastases in LNLs I, II, III, IV and V for early t-stages in oral cavity subsites C02 (tongue), C03 (gum), C04 (floor of mouth), C05 (palate) and C06 (other parts of mouth). The red line marks the 5% threshold for high risk of involvement.

References

[1] Mukherji, S.K., Armao, D., Joshi, V.M.: Cervical nodal metastases in squamous cell carcinoma of the head and neck: What to expect. Head and Neck **23**(11), 995–1005 (2001) https://doi.org/10.1002/hed.1144

[2] Shah, J.P., Candela, F.C., Poddar, A.K.: The patterns of cervical lymph node metastases from squamous carcinoma of the oral cavity. Cancer **66**(1), 109–113 (1990) https://doi.org/10.1002/1097-0142(19900701)66:1<109::AID-CNCR2820660120>3.0.CO;2-A

[3] Biau, J., Lapeyre, M., Troussier, I., Budach, W., Giralt, J., Grau, C., Kazmierska, J., Langendijk, J.A., Ozsahin, M., O'Sullivan, B., Bourhis, J., Grégoire, V.: Selection of lymph node target volumes for definitive head and neck radiation therapy: A 2019 Update. Radiotherapy and Oncology **134**, 1–9 (2019)

https://doi.org/10.1016/j.radonc.2019.01.018

[4] Ludwig, R., Hoffmann, J.-M., Pouymayou, B., Morand, G., Däppen, M.B., Guckenberger, M., Grégoire, V., Balermpas, P., Unkelbach, J.: A dataset on patient-individual lymph node involvement in oropharyngeal squamous cell carcinoma. Data in Brief **43**, 108345 (2022) https://doi.org/10.1016/j.dib.2022.108345

[5] Ludwig, R., Schubert, A., Barbatei, D., Bauwens, L., Werlen, S., Elicin, O., Dettmer, M., Zrounba, P., Balermpas, P., Pouymayou, B., Grégoire, V., Giger, R., Unkelbach, J.: A multi-centric dataset on patient-individual pathological lymph node involvement in head and neck squamous cell carcinoma. Data in Brief, 110020 (2023) https://doi.org/10.1016/j.dib.2023.110020

[6] Ludwig, R., Pouymayou, B., Balermpas, P., Unkelbach, J.: A hidden Markov model for lymphatic tumor progression in the head and neck. Scientific Reports **11**(1), 12261 (2021) https://doi.org/10.1038/s41598-021-91544-1

[7] Batth, S.S., Caudell, J.J., Chen, A.M.: Practical considerations in reducing swallowing dysfunction following concurrent chemoradiotherapy with intensity-modulated radiotherapy for head and neck cancer. Head Neck **36**, 291–298 (2014) https://doi.org/10.1002/hed.23246

[8] Ludwig, R., Hoffmann, J.-M., Pouymayou, B., Däppen, M.B., Morand, G., Guckenberger, M., Grégoire, V., Balermpas, P., Unkelbach, J.: Detailed patient-individual reporting of lymph node involvement in oropharyngeal squamous cell carcinoma with an online interface. Radiotherapy and Oncology **169**, 1–7 (2022) https://doi.org/10.1016/j.radonc.2022.01.035

[9] Ludwig, R.: Modelling lymphatic metastatic progression in head and neck cancer. PhD thesis, University of Zurich, Zurich (2023)

[10] De Bondt, R., Others: Detection of lymph node metastases in head and neck cancer: A meta-analysis comparing US, USgFNAC, CT and MR imaging. Eur. J. Radiol. **64**, 266–272 (2007) https://doi.org/10.1016/j.ejrad.2007.02.037

[11] Ludwig, R., Pouymayou, B., Balermpas, P., Unkelbach, J.: A dynamic model for lymphatic progression of cancer through the head & neck. In: ESTRO, Madrid, p. 75 (2021)

[12] Bishop, C.M.: Pattern Recognition and Machine Learning. Information Science and Statistics. Springer, New York (2006)